A Statistical Analysis of TIR Anomalies Extracted by RST in Relation to an Earthquake in the Sichuan Area using MODIS LST Data

Ying Zhang[1,2], *Qingyan Meng*[1]

1. Institute of Remote Sensing and Digital Earth, Chinese Academy of Sciences, Beijing, 100101, China

2.   University of Chinese Academy of Sciences, Beijing, 100101. China

Abstract: Research in the field of earthquake prediction has a long history, but the inadequacies of traditional approaches to the study of seismic threats have become increasingly evident. Remote sensing and earth observation technology, an emerging method that can rapidly capture information concerning anomalies associated with seismic activity across a wide geographic area, has for some

10   time been believed to be the key to overcoming the bottleneck in earthquake prediction studies. However, a multi-parametric method appears to be the most promising approach for increasing the reliability and precision of short-term seismic hazard forecasting, and thermal infrared (TIR) anomalies are important earthquake precursors. While several studies have investigated the correlation among TIR anomalies identified by the robust satellite techniques (RST) methodology

15   and single earthquakes, few studies have extracted TIR anomalies over a long period within a large study area. Moreover, statistical analyses are required to determine whether TIR anomalies are precursors to earthquakes. In this paper, RST data analysis and the Robust Estimator of TIR Anomalies (RETIRA) index were used to extract the TIR anomalies from 2002 to 2018 in the

20   Sichuan region using Moderate Resolution Imaging Spectroradiometer (MODIS) land surface temperature (LST) data, while the earthquake catalog was used to ascertain the correlation between TIR anomalies and earthquake occurrences. Most TIR anomalies corresponded to earthquakes, and statistical methods were used to verify the correlation between the extracted TIR anomalies and earthquakes. This is the first time that the ability to predict earthquakes has been evaluated based on

25   the positive predictive value (PPV), false discovery rate (FDR), true-positive rate (TPR) and false-negative rate (FNR). The statistical results indicate that the prediction potential of RST with use of MODIS is limited with regard to the Sichuan region.

Key Words: Thermal infrared anomalies, land surface temperature, MODIS, earthquake

1. Introduction

Changes in the surface temperature of the earth's crust prior to the occurrence of earthquakes have been attested to by numerous observations (Tronin et al., 2002). Thermal infrared (TIR) remote sensing has recently emerged as a promising technique for detecting seismic precursors. Anomalous TIR emissions have been detected by satellite sensors prior to the occurrence of major earthquakes (Piroddi et al., 2014). Several studies have detected space-time anomalies in TIR satellite imagery, ranging from weeks to days both before and after earthquakes (Wang, 1984; Gorny et al., 1988; Qiang et al., 1991; Tronin, 1996; Tramutoli et al., 2001; Ouzounov and Freund, 2004; Tramutoli et al., 2015). The investigation of TIR signals as seismic precursors has gained traction worldwide, particularly in Russia, China, India, the United States, and Italy, while Saraf et al. observed similar short-term anomalies in the epicentral regions of earthquakes in India, Algeria, Iran, China, Pakistan and Indonesia using National Oceanic and Atmospheric Administration Advanced Very High Resolution Radiometer (NOAA-AVHRR), Terra/Aqua-Moderate Resolution Imaging Spectroradiometer (MODIS) and passive microwave Defense Meteorological Satellite Program Special Sensor Microwave/Imager (DMSP-SSM/I) satellite data, applying the term 'transient TIR anomalies (Saraf et al., 2009).

There are few analytical techniques that can isolate residual TIR variations potentially associated with earthquake occurrence from TIR signals of normal variability attributable to other causes (Tramutoli et al., 2005). However, in over 10 years (since 2001) of applying the general robust satellite techniques (RST) (Tramutoli, 1998; Valerio, 2005; Tramutoli, 2007) methodology to the investigation of this issue, the potential of this approach for discriminating anomalous TIR signals potentially associated with seismic activity from normal fluctuations in Earth's thermal emissions related to other causes (e.g., meteorological), independent of seismic activity, has been verified (Eleftheriou et al., 2016). RST is based on the Robust AVHRR Technique (RAT), which was developed for environmental monitoring using NOAA/AVHRR observations (Tramutoli, 1998). Since that time, most reported applications of RAT have demonstrated the technique's reliability and exportability for different satellite sensors and geographic areas, and RAT has evolved into RST (Tramutoli, 2007). RST comprises two main steps: the first is characterization of behavior under normal conditions; and the second is establishment of the change-detection criteria that should be

specified for each class of phenomenon considered, and for the selected technology and the time and place of the observation (Tramutoli, 2007).

Several studies have used RST to extract and analyze the space-time distribution of TIR anomalies (henceforth, all TIR anomalies mentioned were extracted using RST) relating to different earthquakes. Using MODIS land surface temperature (LST) data, Pergola et al. studied the 6 April 2009 Abruzzo earthquake and found that spatially extended and time-persistent TIR anomalies (Robust Estimator of TIR Anomalies [RETIRA] > 3) occurred with some degree of space-time correlation with earthquakes of various magnitudes that had occurred in Italy during the period under consideration (15 March–15 April), and from 7 days prior to the main shock in Abruzzo (Pergola et al., 2010). Meanwhile, Bellaoui et al. studied the 21 May 2003 Boumerdes earthquake and detected a TIR anomaly that had persisted for 1 week during the preceding month (Bellaoui et al., 2017). Several studies have also used data from other satellites: Aliano et al. used 8 years' worth of Meteosat TIR observations to analyze the 21 May 2003 Boumerdes/Thenia (Algeria) earthquake and found that the area of interest was affected by significant positive thermal anomalies (S/N > 2.5–3) around 1 month before the main shock (Aliano et al., 2007), while Lisi et al. studied the 6 April 2009 Abruzzo earthquake using NOAA/AVHRR TIR observations and identified TIR anomalies that had some degree of space-time correlation with the Abruzzo earthquake's epicenter between 30 March and 1 April (Lisi et al., 2010). Genzano et al. also studied the 2009 Abruzzo event using different satellite data (5 years of Meteosat Second Generation/Spinning Enhanced Visible and Infrared Instrument [MSG/SEVIRI] observations, 15 years of NOAA/AVHRR observations, and 8 years of Earth Observation System [EOS]/MODIS observations), but no similar results have been observed (Genzano et al., 2010). In addition to analyzing the TIR anomalies for a single earthquake, Tramutoli et al. studied the causes of TIR anomalies: a test over an area affected by variable gas emissions, to determine the correlation between TIR anomalies and seismicity, found that general gas dispersion models and spatial features lend support to the hypothesis of a robust relationship between greenhouse gas emissions and TIR anomalies related to seismic activity(Tramutoli, Aliano et al., 2013).

Several researchers have conducted long-term statistical analyses to determine the correlation between TIR anomalies and earthquakes. Genzano et al. used GMS-5/VISSR TIR measurements to investigate earthquakes with M > 4 that occurred in a wide area surrounding Taiwan, during the

month of September from 1995 to 2002; the false-positive rate (FPR) remained at zero when earthquakes with M > 4 or 4.5 were considered, and the FPR remained under 6% when a threshold of   M > 5 was applied (Genzano, Filizzola et al., 2015). Tramutoli et al. studied earthquakes with M > 4 in the southern Apennines in Italy's Po plain from July 2012 to June 2013 and found that the FPR was less than 33%, while the missing rate was as high as 67% (Tramutoli, Corrado et al., 2015). Eleftheriou et al. studied earthquakes that occurred in Greece between 2004 and 2013 using TIR images acquired with MSG/SEVIRI, and found that more than 93% of all identified TIR anomalies occurred in the prefixed space-time window around the time and location of earthquakes with M > 4, with an overall FPR < 7% (Eleftheriou, Filizzola et al., 2016). It seems that RST is an effective means of extracting TIR anomalies that occur as precursors to earthquakes, but no such study has hitherto been conducted on the Chinese mainland.

Several studies, however, have proven that some individual earthquake results are unreliable. Some so-called TIR anomalies are caused by meteorological anomalies that are unrelated to earthquakes. For example, Matthew et al. studied the Gujarat (India) earthquake of 2001, and found that previous studies, which had indicated the presence of TIR anomalies prior to the earthquake, were unreliable. They concluded that there was no robust evidence for the existence of LST anomalies prior to the 2001 Gujarat earthquake, and that cloud cover was a possible cause of the anomalies (Blackett et al., 2011). As such, rigorous statistical analyses of TIR anomalies over long periods are necessary.

In this paper, RST is applied to a mountainous area in China. Long-term analysis (from Sept. 2002 to Mar. 2018) is used to verify the correlation between TIR anomalies and earthquakes. Based on the statistical results, the earthquake prediction potential of RST will be evaluated.

2.   Study area
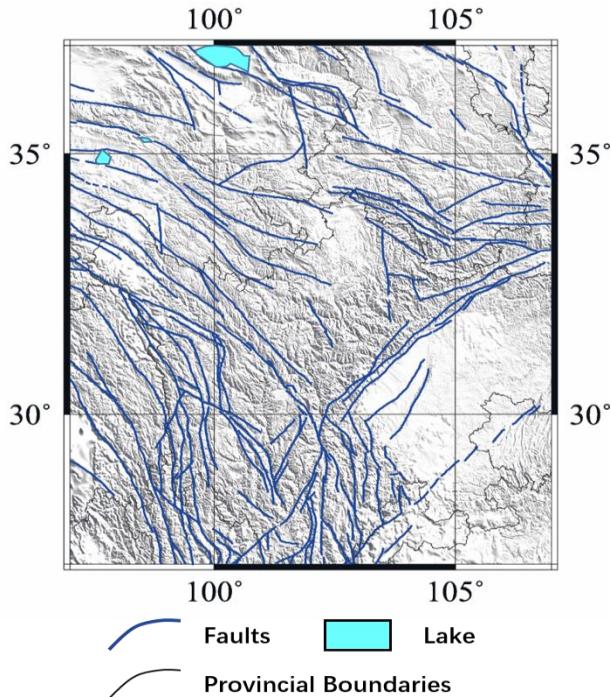
Fig.1 The distribution of faults in East-Southern Gansu province and its neighboring regions.

The southeastern Gansu province and its neighboring regions were selected as the study area, to assess the correlation between TIR anomalies and earthquakes from September 2002 to March 2018. As shown in Fig.1, the range of the study area is $27°N$ to $37°N$, $97°E$ to $107°E$. The study region is located at the intersection of Gansu, Qinghai, and Sichuan provinces; it also includes the intersection of the northern section of the north-south seismic belt and the Kuma seismic belt. Structures in this area are complex and strong earthquakes are frequent (Yang, Zhang et al., 2002). The area is on the eastern edge of the Tibetan Plateau, belonging to the upper part of the rhombic block in the southeast Gansu province. The Xian River fault, the Longmen Shan Fault, and the Anning River fault intersect here, and the structure is Y-shaped. This type of geomorphology is widely encountered in plate tectonics, and the Longmen Shan fault in the north-northeast direction becomes a steep slope in the southeast Sichuan Basin and an erosion plateau northwest of the study area.

3. Data and method

3.1 Data introduction

MODIS data are used to calculate the TIR anomalies, and the earthquake information used for

statistical analysis was provided by China Earthquake Datacenter (http://data.earthquake.cn).

The MODIS instrument is used on both the Terra and Aqua spacecrafts. It has a swath width of 2,330 km and views the Earth's entire surface every 1 to 2 days. Its detectors measure 36 spectral bands between 0.405 and 14.385 μm, and it can acquire data at three spatial resolutions: 250, 500, and 1,000 m. In this study, nighttime MODIS LST daily data (MYD11C1) are used to extract TIR anomalies. Because LST data are susceptible to solar radiation during the daytime, nighttime data are selected for use. The LST data were retrieved at 5,600 m using the generalized split-window algorithm. In the day/night algorithm, daytime and nighttime LSTs are retrieved from pairs of day and night MODIS observations in seven TIR bands. Moreover, the daily nighttime cloud mask data (MYD35L2) are used to exclude the LST data covered by the cloud. The resolutions of the cloud mask data are 250 and 1,000 m, so the resolution must be downscaled to correspond with the LST data.

Earthquakes caused by block movement and crust compression represent an extreme type of geological movement; earthquakes are instantaneous bursts of accumulated energy, and they may result in the presence of TIR anomalies across a large area. Earthquake occurrences within the study area will also cause TIR anomalies close to its boundaries; therefore, for the earthquakes that occurred within the area $25°N$ to $40°N$, $95°E$ to $110°E$ will also be analyzed to examine the TIR anomalies at $27°N$ to $37°N$, $97°E$ to $107°E$. However, earthquakes attributed to ground subsidence and anthropogenic factors are not associated with TIR anomalies, and therefore earthquakes where depth = 0 are excluded from analysis. Tronin et al. observed that anomalies were sensitive to crustal earthquakes with a magnitude of more than 4.7 and over a distance of up to 1,000 km (Tronin et al., 2002). Therefore, we selected earthquakes of M ≥ 3.5 and depth > 0 that occurred within the area of $25°N$ to $40°N$, $95°E$ to $110°E$ for analysis, and after screening, a total of 3,615 earthquakes satisfied these conditions.

3.2 RST Methodology

The RST approach is based on multi-temporal analyses of historical satellite observational datasets acquired under similar observational conditions (Eleftheriou et al., 2016). Since the surface environment is relatively constant, high- and low-temperature locations are also relatively consistent. Over time, the infrared brightness temperature will change, albeit very gradually and in small

increments with obvious seasonal characteristics. Aside from the influences of meteorological factors and earthquake TIR anomalies, the brightness temperature within the same area and during the same time period exhibits robust stability and regularity. Therefore, the basic principle that guides RST is that the background field is constructed to extract the thermal anomalies, and the mean and variance of the LST are used to evaluate the degree of TIR anomaly.

This method consists of three main steps, as follows:

● Pre-processing

RST is used to construct a reference, which is considered to be in a normal state under no influence from other factors, and to measure and extract the anomalies at the corresponding time. $V(r,t)$ are LST data in location r at time t. Therefore, the first step is to eliminate the data affected by clouds, and to remove outliers.

➤ To eliminate the effect of day-to-day climatological changes or seasonal time drifts, pre-processing is applied to the daily LST data:

$$\Delta V(r, t) = V(r, t) - V(t) \quad (1)$$

Where $\Delta V(r, t)$ is the difference between the value of LST acquired at time t in location r and its spatial average, $V(t)$, computed in the investigated area considering only those pixels belonging to the same class; in this study area, all pixels belong to the land class.

➤ The cloud mask is constructed using cloud mask data (MYD35L2). To ensure that only cloud-free radiances contribute to the computation of the reference fields (RFs), not only those pixels but also the 24 pixels in the surrounding 5×5 area (frequently belonging to cloud edges) are excluded from the following RFs computations (Eleftheriou et al., 2016).

$$A_1(r, t) = \begin{cases} 0, if \ the \ location \ r \ was \ affected \ by \ clouds \ at \ time \ t \\ 1, otherwise \end{cases} \quad (2)$$

➤ An outlier-mask is constructed.

This step is to determine the outliers, and these values should be excluded from the construction of the background field and the extraction of TIR anomalies.

$$A_2(r, t, \tau) = \delta_1(r, t, \tau) * \delta_2(r, t, \tau) * \delta_3(r, t, \tau) \quad (3)$$

As it is shown in eq. (3), $\delta_1, \delta_2, \delta_3$ are three kinds of data that should be excluded from the construction of backfields. As demonstrated by Aliano et al. and Genzano et al., the spatial distribution of clouds over a thermal heterogeneous scene can significantly change the value

of ΔV in the cloud-free pixels(Aliano et al., 2008; Genzano et al., 2009). The large cloud cover area will introduce a cold spatial average effect to the computation of the RFs, so that when $V(r,t) < \mu_V - 2 * \sigma_V$ (here, μ_V is the temporal average and the σ_V is its standard, these pixels' values will be excluded, Eleftheriou et al., 2016).

$$\delta_1(r,t,\tau) = \begin{cases} 0, if \ V(r,t) - \mu_V(r,\tau,T) < -2 * \sigma_V(r,t,\tau), t < \tau \\ 1, otherwise \end{cases} \quad (4)$$

Moreover, even where no cold spatial average effect is produced, extended cloud coverage can determine the $V(t)$ values and the values of the considered signal $\Delta V(r,t)$, scarcely representative of the actual conditions of cloud-free pixels, so that when the cloudy fraction of the land portion of the scene is $> 80\%$, all pixels must be excluded from the computation of the RFs (Eleftheriou et al., 2016).

$$\delta_2(r,t,\tau) = \begin{cases} 0, if \ cloudy \ fraction \ of \ land \ portion \ of \ scene \ is \ > 80\% \\ 1, otherwise \end{cases} \quad (5)$$

δ_3 is used to remove the outliers (where $k \geq 2$), and its expression is as follows:

$$\delta_3(r,t,\tau) = \begin{cases} 1, if \ |V(r,t) - \mu_V(r,\tau,T)| < k\sigma_V(r,t,\tau) \\ 0, otherwise \end{cases} \quad (6)$$

$\delta(r,t,\tau) = \delta_1(r,t,\tau) * \delta_2(r,t,\tau) * \delta_3(r,t,\tau)$ computed using an iterative $k\sigma$-clipping technique, which begins by computing $\delta(r,t,\tau)$ based on the first determination of $\mu_V(r,\tau,T)$ and $\sigma_V^2(r,\tau,T)$, and continues by updating their values using only space-time locations with $\delta(r,t,\tau) = 1$, as follows:

$$\mu'^2_{\Delta V}(r,\tau,T) \equiv \frac{\sum_{\forall t \in T}[\Delta V(r,t) \cdot A(r,t)]}{\sum_{\forall t \in T} A(r,t)} \quad (7)$$

$$\sigma'^2_{\Delta V}(r,\tau,T) \equiv \frac{\sum[\Delta V(r,t) \cdot A(r,t) - \mu_{\Delta V}(r,\tau)]^2}{\sum_{\forall t \in T} A(r,t)} \quad (8)$$

The process should be iterated until no further exclusions are determined, using the latest determination of δ (Tramutoli, 1998). And the final result of δ is the A_2 what we want.

- Computing Reference Fields

  ➢ The $\mu_{\Delta V}(r,\tau,\Delta T)$ is the mean of location r for time series T. The variance $\sigma^2_{\Delta V}(r,\tau,T)$ is applied at time τ using homogeneous historical records collected under the temporal constraint $t \in T$ $(t < \tau)$ and the $V_{REF}(r,\tau,\Delta T)$ is the background field.

$$A(r,T) = A_1(r,t) * A_2(r,t) \quad (9)$$

$$V_{REF}(r,\tau,T) \equiv \frac{\sum_{\forall t \in T}[\Delta V(r,t) \cdot A(r,t)]}{\sum_{\forall t \in T} A(r,t)} \quad (10)$$

$$\sigma^2_{\Delta V}(r,\tau,T) \equiv \frac{\sum[\Delta V(r,t)\cdot A(r,t)-\mu_{\Delta V}(r,\tau)]^2}{\sum_{\forall t \in T} A(r,t)} \quad (11)$$

- Change-detection

  ➢ The RETIRA (Robust Estimator of TIR Anomalies, Filizzola, 2004) must be computed, and the bigger the absolute value is, the more evident the anomaly is. $\otimes_{\Delta V}(r,\tau,T)$ is the RETIRA of location r at time τ, which belongs to the time series T.

$$\otimes_{\Delta V}(r,\tau,T) = \frac{[\Delta V(r,\tau) - V_{REF}(r,\tau,T)]}{\sigma_{\Delta V}(r,\tau,T)} \quad (12)$$

  ➢ Whether $\otimes_{\Delta V}(r,\tau,T)$ is affected by cloud should be determined. From the results, it may easily be concluded that some areas will lack data at certain times, and for these scenarios a special value must be implemented to indicate that these data are affected by clouds and should be excluded from the ensuing analyses.

3.3 Identification of TIR anomalies

After the calculation of $\otimes_{\Delta V}(r,\tau,T)$, the next step is to identify the TIR anomalies and correlate them with earthquake occurrences. In this paper, a $\otimes_{\Delta V}(r,\tau,T)$ that exceeds the threshold indicates the presence of a TIR anomaly; further conditions will be applied to confirm the correlation. For $\otimes_{\Delta V}(r,\tau,T)$ and $eq(r,t)$, only in those cases where the following conditions are satisfied can it be concluded that the TIR anomaly is related to $eq(r,t)$:

1) The RETIRA $\otimes_{\Delta V}(r,\tau,T)$ > 2. In Eleftheriou's study, the threshold was set at 4 (Eleftheriou et al., 2016) ; however, from a statistical perspective, when the value is greater than two times the standard deviation, it already falls within the abnormal category. In this study, therefore, the threshold is set at 2.

2) The $V(r,t)$ is not blocked by clouds or affected by other factors.

3) Spatial persistence: The TIR anomalies cluster together and are not isolated, being part of a group covering at least 150 km^2 within an area of $1° * 1°$ (400 pixels in the images).

4) Temporal persistence: At least one more TIR anomaly appears within 7 days after the first TIR anomaly.

5) The TIR anomalies appear 30 days before or 15 days after the $eq(r,t)$ (Eleftheriou et al., 2016) .

6) The shortest distance from a given point in the TIR anomalies group to the epicenter of $eq(r,t)$ is less than $R_D = 10^{0.43M}$.

Where the TIR anomalies satisfy conditions 1), 2), 3) and 4), but do not satisfy at least either 5) or 6), TIR anomalies are present with no corresponding earthquake. There are also cases wherein no TIR anomalies occur.

4. Results and analysis

A comprehensive statistical analysis and the TIR extraction results are detailed in this chapter. In chapter 4.1, a statistical analysis is conducted to ascertain the basic seismological conditions in the study area, while the statistical results for the correlation between earthquakes and TIR anomalies are presented and analyzed in chapter 4.2. Finally, an analysis of the earthquake prediction potential of RST is presented in chapter 4.3.

4.1 Statistical analysis of earthquake activity in the study area

Prior to investigating the correlation between TIR anomalies and earthquakes, a simple analysis of the temporal and spatial characteristics of the earthquakes is required.

First, the temporal distribution shows that the seismicity from 2002 to 2018 was most active in 2008, and that it increased in frequency and violence from that time. The bottom of Fig. 2 indicates that there were 3,615 earthquakes in the study area(3.5 ≤ M ≤ 4, 2,262; 4 ≤ M ≤ 5, 1,124; 5 ≤ M ≤ 6, 198; 6 ≤ M ≤ 7, 26; and 7 ≤ M ≤ 8, 5. Therefore, the study area is characterized by severe seismic activity. As may be seen from the upper part of Fig. 2, the average earthquake frequency during period A (from 2002.09 to 2007.12) was around 78. However, the total number of earthquakes in 2008 increased to 981 including the May 12 2008 Ms 8.0 Wenchuan Earthquake, the most serious earthquake in China in recent years. Although the frequency decreased substantially after 2008 (the average frequency during this period was 243), it remained much higher than it had been during period A. The temporal distribution indicates that seismic activity prior to 2008 had been relatively weak, but in 2008, the seismic activity was extremely intense and reached its peak. After 2008, seismicity in this area continued to maintain this intensity.
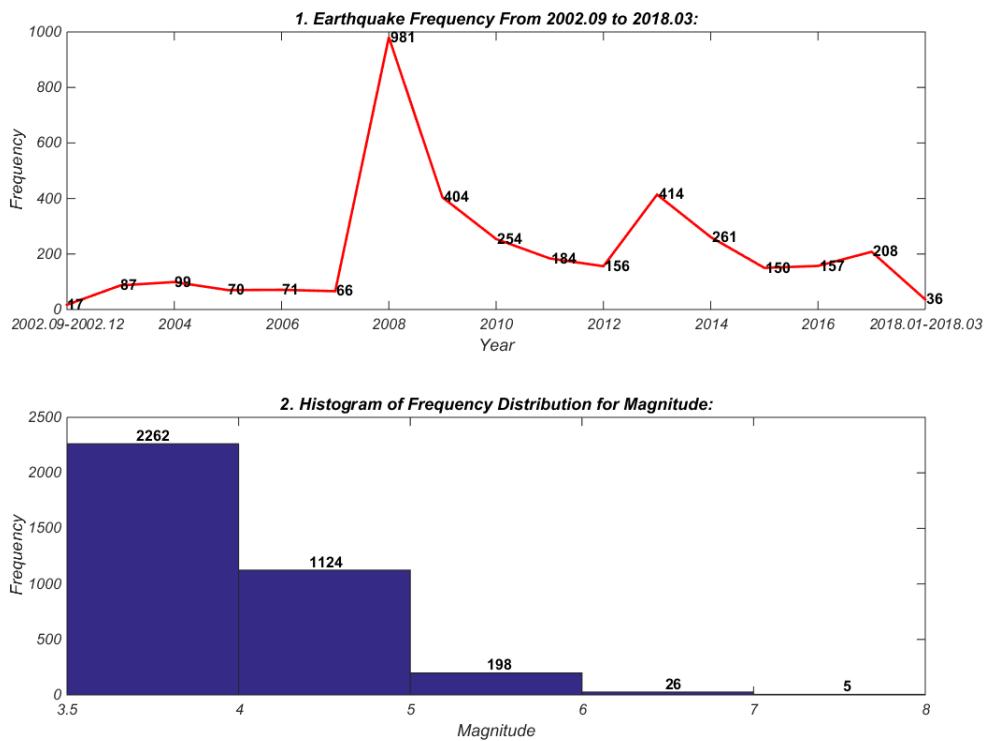
Fig. 2 The temporal distribution from 2002.09 to 2018.03 of earthquakes with $M \geq 3.5$ in the study area, and the distribution of seismic frequency with earthquake magnitude.

Table 1 Catalog of earthquakes with $M \geq 5.0$ prior to 2008

Date	Latitude\°N	Longitude\°E	Depth\km	Magnitude
2003.07.21	25.95	101.23	6	6.4
2003.10.16	25.92	101.30	5	6.2
2003.10.25	38.35	100.93	13	6.1
2003.08.18	29.57	95.60	33	6
2003.10.25	38.32	100.97	10	6
2006.07.19	33.03	96.35	30	5.9
2002.12.14	39.82	97.33	22	5.8
2005.08.05	26.55	103.15	21	5.6
2006.03.30	35.50	95.40	18	5.6
2003.11.13	34.75	103.93	10	5.5
2006.07.22	28.02	104.13	9	5.5
2006.08.25	28.03	104.01	7	5.5

2006.06.21	33.07	104.90	15	5.4
2006.07.18	33.07	96.28	20	5.4
2007.07.22	38.35	101.30	19	5.3
2004.09.07	34.73	103.92	19	5.2
2005.09.05	27.18	103.72	10	5.2
2003.08.21	27.42	101.27	5	5.1
2003.10.17	25.97	101.27	7	5.1
2003.11.01	25.93	101.22	3	5.1
2004.11.27	25.17	98.02	12	5
2005.01.05	32.28	101.55	5	5
2005.03.15	25.07	99.08	2	5
2006.07.23	33.03	96.05	30	5

Further evidence is presented in Table 1, where earthquakes of $M \geq 5.0$ that occurred during period A (from 2002.09 to 2007.12) are detailed. There were 229 earthquakes of $M \geq 5.0$, while the total number during period A was 24, which accounted for 10.48% overall; the duration of period A accounted for 33.87% of the total timeframe (i.e., period A + period B). Moreover, there were no earthquakes of $M \geq 6.5$ during period A, but there were 14 earthquakes of $M \geq 6.5$ during period B (from 2008.01 to 2018.03). All of this evidence indicates that seismic activity during period B was significantly more violent and frequent.
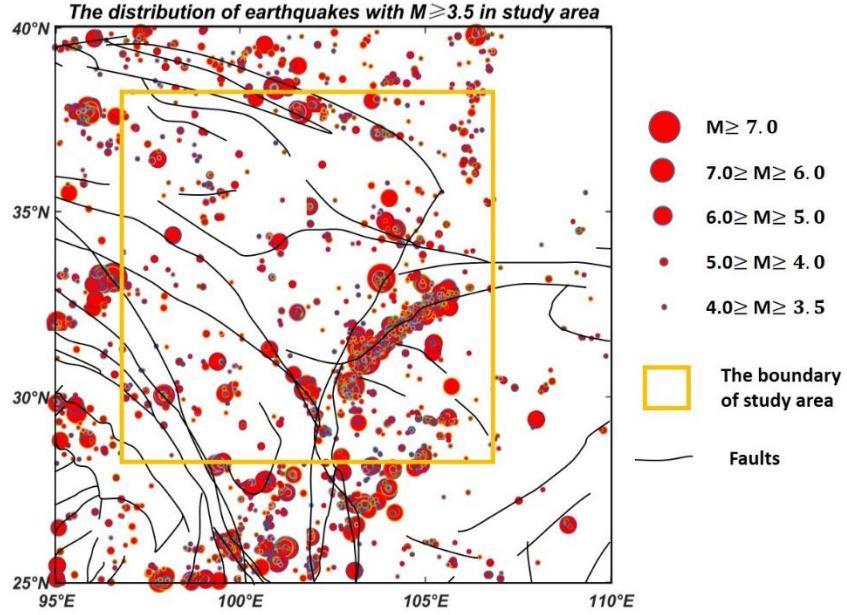
Fig. 3 The spatial distribution of earthquakes in the study area. The orange rectangle represents the study area ($27°N$ to $37°N, 97°E$ to $107°E$). Earthquakes beyond the parameters of the study area are shown because earthquakes close to the study area may also cause TIR anomalies within the study area.

Figure 3 shows the spatial distribution of earthquakes within the study area. The results indicate that seismic events are clustered primarily in the west and center of the study area ($25°N$ to $40°N, 95°E$ to $110°E$) which are mountainous regions. The earthquakes are mainly aggregated along faults, with a much sparser spatial distribution in the east and in the Sichuan Basin. There is a clustering phenomenon centered on earthquakes of M $\geq$ 6, since earthquakes usually occur along the fault lines of active geological movements.

The purpose of investigating the temporal and spatial characteristics of earthquakes is to acquire a general understanding of the seismic activities within the study area. There is another important reason, however, which is to avoid significant accumulation of earthquakes within a short timeframe, and concentrated within a small area, with the result that the same TIR anomaly corresponds to numerous earthquakes; this phenomenon excessively distorts the statistical results presented above. Around 233 earthquakes were observed to occur after the May 12 2008 Ms 8.0 Wenchuan earthquake, in locations close to the epicenter of Wenchuan event. In chapter 4.2, the statistical

analysis will be divided into two sections: one dealing with the earthquakes that occurred during period C (from 2008.04 to 2008.07), and the other dealing with those that occurred outside of period C.

4.2 Statistical analysis of the correlation between TIR anomalies and earthquakes

In this section, TIR anomalies are extracted and a statistical analysis of the correlation between TIR anomalies and earthquakes of M ≥ 4 is conducted. Evaluation of the TIR anomalies conforms strictly to the guidelines detailed in chapter 3.3.
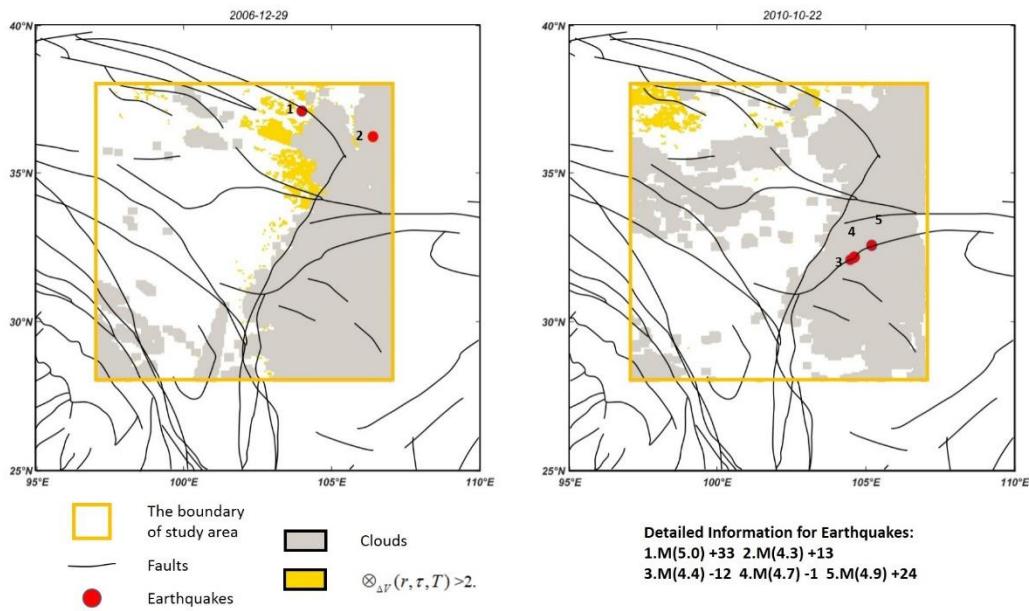
Fig .4 Two examples of the correlation between TIR anomalies and earthquakes: on the left is the TIR anomaly recorded on 2006.12.29 that corresponded to two earthquakes, and on the right is the TIR anomaly recorded on 2010.10.22 that did not correspond to earthquakes.

As shown in Fig. 4, the TIR anomalies are extracted using RST and the identification rules are applied to determine the correlation between TIR anomalies and earthquakes. After
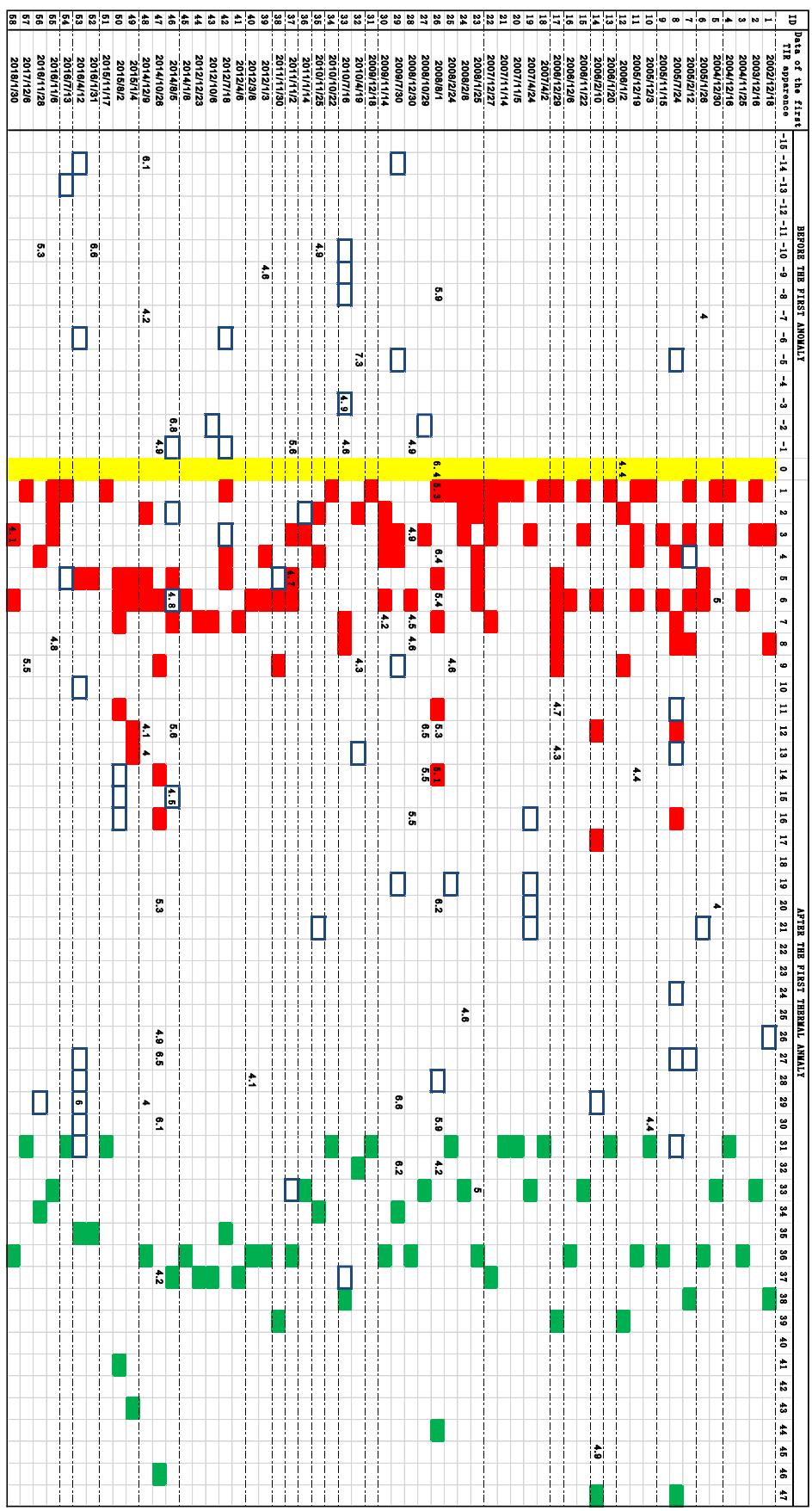
Fig. 5 Correlation analysis among TIR anomalies and earthquakes with magnitude bigger than 4.0 in the Sichuan area from September 2002 to March 2018. All 61 TIR anomalies are identified, and each row corresponds to one TIR anomaly. The first day of the TIR anomaly is shown in yellow, while the red cells denote the ensuing persistence. The cells in the blue rectangle indicate that this day is affected by a large area of cloud cover, and the green cell is the final limitation for each anomaly. Cells with numbers indicate days of occurrence, and magnitude, of seismic events. The rows in the dotted box mean that there is no earthquake corresponding to this TIR anomaly.

extraction, the total number of TIR anomalies is 58 and the correlation results are presented in Fig. 5. Considering the examples reported in Fig. 4, which are summarized in rows 17 and 34, the cells in yellow corresponding to the first day of TIR anomaly are 2006-12-29 and 2010-10-22, respectively. It may be concluded based on Fig. 5 that 30 TIR anomalies correspond to earthquakes, while the other 28 (rows 1, 2, 3, 4, 7, 8, 9, 13, 15, 16, 18, 19, 20, 21, 22, 31, 34, 36, 38, 41, 42, 43, 44, 45, 49, 50, 51 and 54) do not. The correlation rate is 51.7%. It may be seen from Fig. 6 that most TIR anomalies appear as precursors to earthquakes.
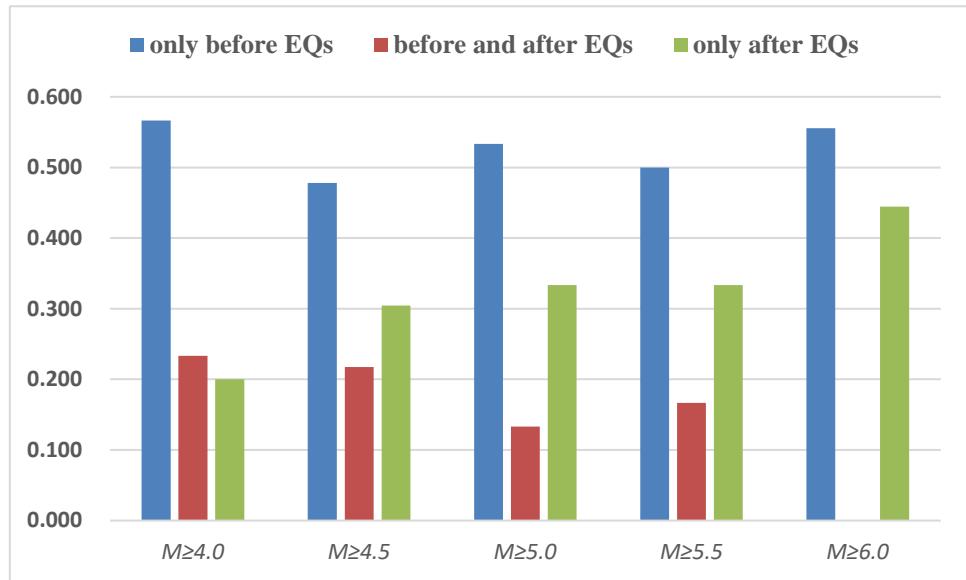
Fig. 6 Distribution of TIR anomalies with respect to earthquake occurrences for different classes of magnitude.

However, as mentioned in section 4.1, period C may be associated with a significant increase in the total number of TIR anomalies and the correlation rate. As such, the experiment was also performed without period C, and the number of TIR anomalies is still 58, while the correlation rate is 51.7%, both of which are the same as the former result. Theoretically, the high earthquake frequency and magnitudes of period C should generate numerous TIR anomalies and correlate strongly with earthquakes. However, only a single TIR anomaly corresponding to five earthquakes was observed. Figure 7 may indicate the reason for this: earthquakes cluster along several faults, but the spatial locations of these faults are always blocked by cloud cover with a percentage in excess of 90%. With the lengthy persistence of cloud coverage over a large area, the TIR anomalies caused by earthquakes during period C cannot be extracted using RST.

Comprehensive analysis of Fig. 5 reveals that there are 22 TIR anomalies in period A, 15 of which do not correspond to earthquakes, while of 36 TIR anomalies in period B, 13 do not correspond to earthquakes and the correlation rate reaches 63.9%, which is significantly higher than 51.7%. Figures 2 and 8 illustrate this phenomenon: in period A, the earthquake intensity magnitudes are small, the frequency is low, and almost half of all earthquakes occur in the cloudy region, or adjacent to it; therefore, it is difficult to determine any correspondence between the earthquakes and the extracted anomalies, and some anomalies may have not been extracted owing to the cloud cover. Regarding the results from period B, the frequency and magnitudes of earthquakes in sparsely clouded areas are significantly increased, so that TIR anomalies are more likely to be extracted and more likely to correspond to earthquakes.
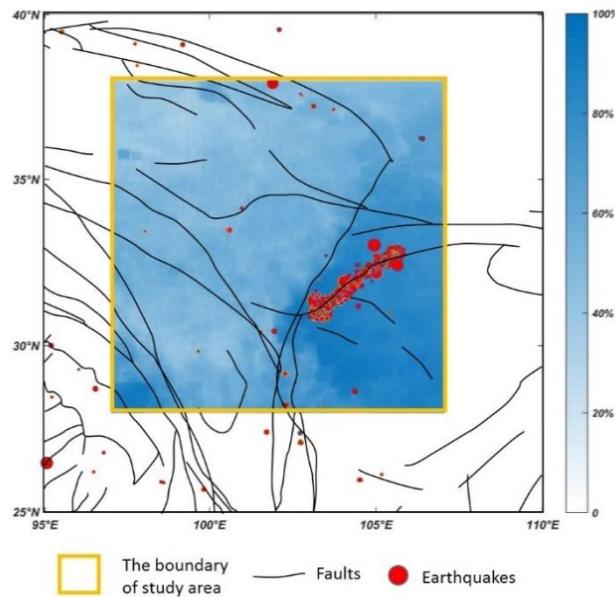
Fig. 7 The distribution of earthquakes and the frequency of each pixel blocked by cloud cover in period C; higher values indicate that the pixels are more frequently blocked by clouds.
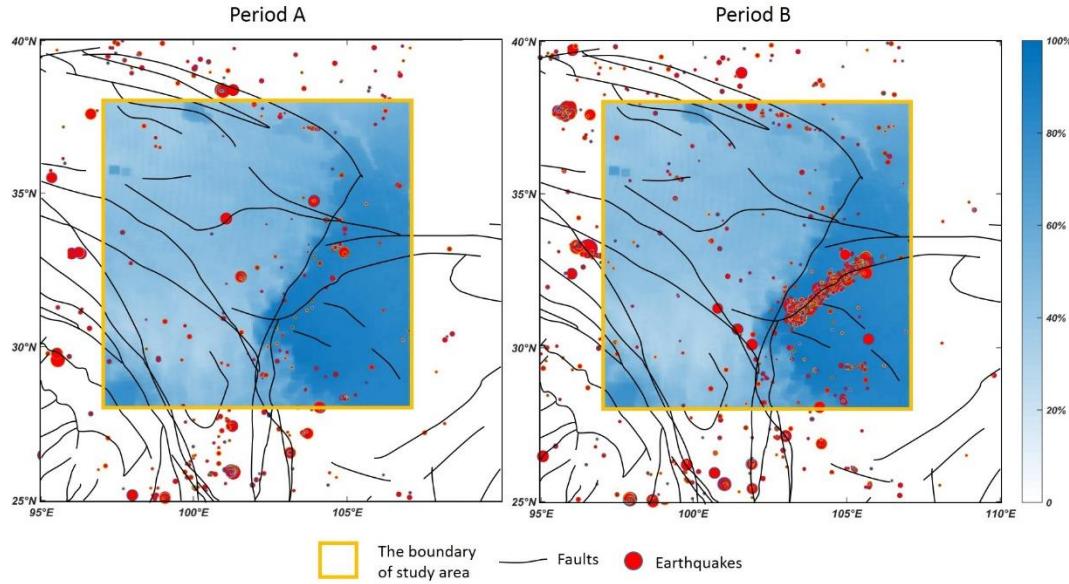
Fig.8 The distribution of earthquakes in periods A and B and the frequency of each pixel being blocked by cloud cover in period C; higher values indicate that the pixels are more frequently blocked by clouds.

4.3 Evaluation of the earthquake prediction potential of RST using MODIS LST data in Sichuan area

With the aim of evaluating the earthquake prediction potential of RST using MODIS LST data for the Sichuan area, the true-positive rate (TPR) of correspondence between TIR anomalies and earthquakes with M ≥ 4.0 alone is insufficient. Therefore, four types of data are incorporated, with four types of ratio calculated as follows:

TP1: True-positive 1, the total number of TIR anomalies that correspond to earthquakes.

FP: False-positive, the total number of TIR anomalies that do not correspond to any earthquakes.

TP2: True-positive 2, the total number of earthquakes that correspond to TIR anomalies.

FN: False-negative, the total number of earthquakes that do not correspond to any TIR anomalies.

Positive predictive value (PPV): The ratio of TIR anomalies that correspond to earthquakes to the total number of TIR anomalies.

False discovery rate (FDR): The ratio of TIR anomalies that do not correspond to any earthquakes to the total number of TIR anomalies.

TPR: The ratio of earthquakes that correspond to TIR anomalies to the total number of

earthquakes.

FNR: The ratio of earthquakes that do not correspond to any TIR anomalies to the total number of earthquakes.

Table 2 Statistical results of earthquakes with M ≥ 5.0

	TP1	FP	TP2	FN
M ≥ 5.0	15	43	27	223
	PPV: 25.9% TP1/(TP1+FP)		TPR: 10.8% TP2/(TP2+FN)	
	FDR:74.1% FP/(TP1+FP)		FNR: 89.2% FN/(TP2+FN)	

For a more accurate understanding of the eight parameters, an example is presented in Table 2. The example considered the earthquakes of M $\geq$ 5.0, and the results indicate that 58 (TP1+FP) TIR anomalies appeared over the duration of the study period, and 15 (TP1) of these correspond to earthquakes while the other 43 (FP) do not; as such, the probability of exact correspondence between TIR anomalies and earthquakes is 25.9% (PPV), while the probability of no correspondence is 74.1% (FDR). Moreover, 250 (TP2+FN) earthquakes of M $\geq$ 5.0 were recorded in the study area; 27 (TP2) of these correspond to TIR anomalies, while the other 223 (FN) do not; as such, the probability of exact correspondence between the earthquakes and TIR anomalies is 10.8% (TPR) while the probability of no correspondence is 89.2% (FNR). We have calculated the earthquakes with M $\geq$ m (m = {3.5, 3.6, 3.7,…,7.8, 7.9, 8.0}), and the experiments are conducted both with and without period C. The results show that these do not differ significantly, so in this section only the results including period C are discussed.
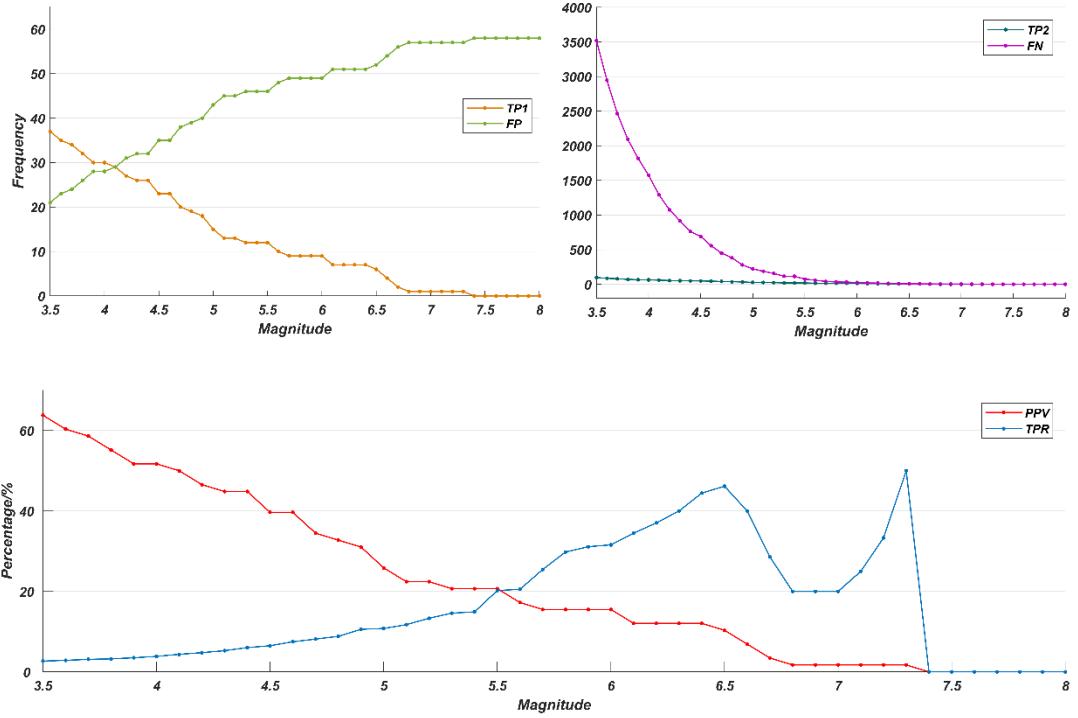
Fig. 9 The statistical results of earthquakes including period C (from 2008.04 to 2008.07), and the curves TP1, FP, TP2, FN, PPV and TPR, which correspond to the examples presented in Table 2.

Table 3 Detailed results of earthquakes including period C (from 2008.04 to 2008.07)

M	TP1	FP	TP2	FN	PPV	FDR	TPR	FNR
3.5	37	21	97	3518	0.638	0.362	0.027	0.973
3.6	35	23	87	2946	0.603	0.397	0.029	0.971
3.7	34	24	79	2465	0.586	0.414	0.031	0.969
3.8	32	26	70	2094	0.552	0.448	0.032	0.968
3.9	30	28	66	1817	0.517	0.483	0.035	0.965
4	30	28	63	1574	0.517	0.483	0.038	0.962
4.1	29	29	59	1291	0.500	0.500	0.044	0.956
4.2	27	31	54	1076	0.466	0.534	0.048	0.952
4.3	26	32	51	917	0.448	0.552	0.053	0.947
4.4	26	32	49	762	0.448	0.552	0.060	0.940
4.5	23	35	48	691	0.397	0.603	0.065	0.935
4.6	23	35	45	556	0.397	0.603	0.075	0.925
4.7	20	38	40	451	0.345	0.655	0.081	0.919

4.8	19	39	37	382	0.328	0.672	0.088	0.912
4.9	18	40	33	279	0.310	0.690	0.106	0.894
5	15	43	27	223	0.259	0.741	0.108	0.892
5.1	13	45	25	188	0.224	0.776	0.117	0.883
5.2	13	45	24	156	0.224	0.776	0.133	0.867
5.3	12	46	20	117	0.207	0.793	0.146	0.854
5.4	12	46	20	114	0.207	0.793	0.149	0.851
5.5	12	46	19	75	0.207	0.793	0.202	0.798
5.6	10	48	15	58	0.172	0.828	0.205	0.795
5.7	9	49	14	41	0.155	0.845	0.255	0.745
5.8	9	49	14	33	0.155	0.845	0.298	0.702
5.9	9	49	14	31	0.155	0.845	0.311	0.689
6	9	49	12	26	0.155	0.845	0.316	0.684
6.1	7	51	10	19	0.121	0.879	0.345	0.655
6.2	7	51	10	17	0.121	0.879	0.370	0.630
6.3	7	51	8	12	0.121	0.879	0.400	0.600
6.4	7	51	8	10	0.121	0.879	0.444	0.556
6.5	6	52	6	7	0.103	0.897	0.462	0.538
6.6	4	54	4	6	0.069	0.931	0.400	0.600
6.7	2	56	2	5	0.034	0.966	0.286	0.714
6.8	1	57	1	4	0.017	0.983	0.200	0.800
6.9	1	57	1	4	0.017	0.983	0.200	0.800
7	1	57	1	4	0.017	0.983	0.200	0.800
7.1	1	57	1	3	0.017	0.983	0.250	0.750
7.2	1	57	1	2	0.017	0.983	0.333	0.667
7.3	1	57	1	1	0.017	0.983	0.500	0.500
7.4	0	58	0	1	0.000	1.000	0.000	1.000
7.5	0	58	0	1	0.000	1.000	0.000	1.000
7.6	0	58	0	1	0.000	1.000	0.000	1.000

7.7	0	58	0	1	0.000	1.000	0.000	1.000
7.8	0	58	0	1	0.000	1.000	0.000	1.000
7.9	0	58	0	1	0.000	1.000	0.000	1.000
8	0	58	0	1	0.000	1.000	0.000	1.000

As may be seen from Fig 9, PPV declines as the magnitude increases, while FP is also clearly seen to increase. This phenomenon indicates that with increased magnitude, the number of TIR anomalies that correspond to the earthquakes decreases. TPR and FN can be seen to decrease steadily as the total number of earthquake samples decreases.

The ratios (PPV and TPR) demand closer attention, however. First, a general perceptual analysis reveals that PPV decreases steadily as M increases, while TPR increases when M≤ 6.5 and M=6.8~7.3 ≤ 6.6 and M = 7.2, 7.3; the maximum TPR is 50% when M = 7.3, and TPR decreases when M=6.5~6.8 = 6.7~7.1. When M is 3.5 and 4.0, PPV is 63.8% and 51.7%, respectively, indicating that when a TIR anomaly is evident, there is a 63.8% (51.7%) possibility that earthquakes of M ≥ 3.5 (4.0) will occur. When M is 5, 6, or 7, PPV is 25.9%, 15.5%, 1.7%, and these are much lower than the PPV of M = 3.5 and 4.0. It may be concluded from the change in the PPV curve that where a TIR anomaly is present, there will be a more than 50% possibility of an earthquake with M ≥3.5 (4.0) in the study area. It does not necessarily follow, however, that when there is a TIR anomaly, there will be strong earthquakes with M ≥ 5.0 in the study area. On the contrary, the probability that earthquakes of high magnitude will occur remains low.

The TPR curve indicates the probability that an associated TIR anomaly will be present when earthquakes occur. When M =3.5 the TPR is 2.7%, and as M increases, TPR increases steadily, although it remains low when M ∈ [3.5, 5.4] and the TPR is lower than 20%. The results show that lower-magnitude earthquakes are relatively less likely (less than 20%) to correspond to TIR anomalies, while earthquakes of M ≥ 6.0, which are very destructive, have a relatively high likelihood of corresponding. High correspondence is particularly significant with regard to earthquake prediction: it indicates that destructive earthquakes are considerably more likely to be predictable in this case.

According to both sets of results, we may conclude that when a TIR anomaly is present, there is a 51.7% possibility that an earthquake of M ≥ 4.0 will occur, and in the case of earthquakes of M

≥ 6.0 occurs, more than one third correspond to TIR anomalies. Most TIR anomalies correspond to earthquakes of M ≥ 4.0. However, when M ≥ 6.0, the PPV is relatively low, resulting in a higher false alarm rate for strong earthquakes. TPR increases with magnitude, and when M = 7.3, it is 50%. It may be concluded based on the TPR curve that the greater an earthquake's magnitude, the more effective this method is likely to be in predicting it. However, the PPV and TPR are low, or the FDR and FNR, which are negative with regard to the predictive potential of RST, are high. Overall, the false alarm rate for M ≥ 4.0 is 48.3%, and as M increases so too does FDR. The missing rate for M ≥ 4.0 is 96.2%, and it seems that when M < 5.5, there is no obvious correlation between TIR anomalies and earthquakes; nevertheless, TPR tends to increase when M increases, though its maximum remains at 50%, which is also an unsatisfactory value. As such, the prediction potential of RST using MODIS LST data in the Sichuan area is limited. However, it doesn't indicate that the RST is not effective for earthquake prediction, on the contrary, many other cases prove that this method is very effective for extracting TIR anomalies. The low PPV and TPR may be caused by the limitation of RST, nature of MODIS LST data, special topographic and weather background of study area, or something else.

5. Discussion

To compare these results with those from previous similar studies, a summaries of four such studies are presented in Table 3. It is evident that PPV is relatively lower in this study than in the others, so it is important to verify its actual added value in comparison with a random alarm function (see, for example, Eleftheriou et al., 2016). The detailed method is available in chapter 3.4 of Eleftheriou et al. (2016), and the result is presented in Fig. 10. When M ≥ 3.5, the point is at the upper extreme of the random guess, with the result that there is no obvious correlation between TIR anomalies and earthquakes with M ≥ 3.5; rather, the correlation appears to be casual. When M ≥ 4.0 and M≥ 4.5, both of these points are still very close to the line, though at the lower part, meaning that a non-casual correlation is actually present among the extracted TIR anomalies and earthquakes (M ≥ 4.0 and ≥ 4.5). However, the correlation is not strong. The result in this study is different from that achieved by Eleftheriou: in her study, the strong correlation between the TIR anomalies and earthquakes is much more evident. This may be attributable to the fact that, as shown in Fig. 8, the east and southeast corner of the study area is consistently blocked by clouds, i.e., for

over 90% of the time. Several earthquakes also occur in this area, but insufficient data prevents correlation between the earthquakes and TIR anomalies, and they are inevitably classified into FNR, which is v in Molchan error analysis, making the correlation weaker. For M $\geq 5.0, 5.5$ and 6.0, the points are clear under the random guess, and as M increases, the non-causal correlation is strengthened.

Tronin indicated that the anomaly was sensitive to crustal earthquakes that were of a magnitude greater than 4.7 over a distance of up to 1,000 km (Tronin, Hayakawa et al., 2002). In this study, however, when M = 4.7, the TPR is 9.6% and the FNR is 90.4%, and at the point in Fig. 10 at which M ≥ 4.5 is very close to the random guess, the statistical result does not support the theory that the TIR anomaly is sensitive to the earthquakes of M ≥ 4.7. When M ≥ 5.9, earthquakes appear to be sensitive to TIR anomalies, as may be seen from Table 3. This failure to conform to previous conclusions may be attributable to the regional structure and geological movement, cloud cover, and effectiveness of the method for extracting TIR anomalies, among other factors. Further study is required, however.

Table 4 A general summary of research on the statistical correlation between TIR anomalies and earthquakes

Author	Data Source	Study area	Duration	PPV
Genzano	GMS-5/VISSR	Taiwan	1995.09-2002.09	100%(M$\geq$ 4 or 4.5) 94%(M$\geq$ 5.0)
Tramutoli		Italian southern Apennines	2012.07-2013.06	67%
Eleftheriou Alexander	MSG/SEVIRI	Greece	2004-2013	93% (M$\geq$ 4.0)
Ying Zhang	MODIS	China, Sichuan Area	2002.09-2018.03	51.7%(M$\geq$ 4.0)

We calculated the total number of TIR anomalies and numbers of FP for each month in both studies, and found that in Eleftheriou's study TIR anomalies clustered in November, September, January and February, while in the present study they cluster in November, September and January.

A line indicating the percentage of area not blocked by clouds in the Sichuan region is also illustrated in Fig. 11. In this paper, there is a significant positive proportional correlation between the number of TIR anomalies and the area not blocked by clouds. When the percentage is high, the number of TIR anomalies is also high, and when the percentage is low, the number of TIR anomalies is low. Therefore, while several TIR anomalies related to earthquakes may be present, they are blocked by cloud cover and cannot be extracted. However, the question of what the true cause is, i.e., cloud clover, seasonal weather, or some other factor, remains to be answered satisfactorily. Moreover, another interesting phenomenon is that several TIR anomalies that do not correspond to any earthquakes cluster in November and September, both of which are cold months that do not tend to be cloudy. Therefore, the clustering of numerous FPs during these 2 months also remains to be fully investigated.
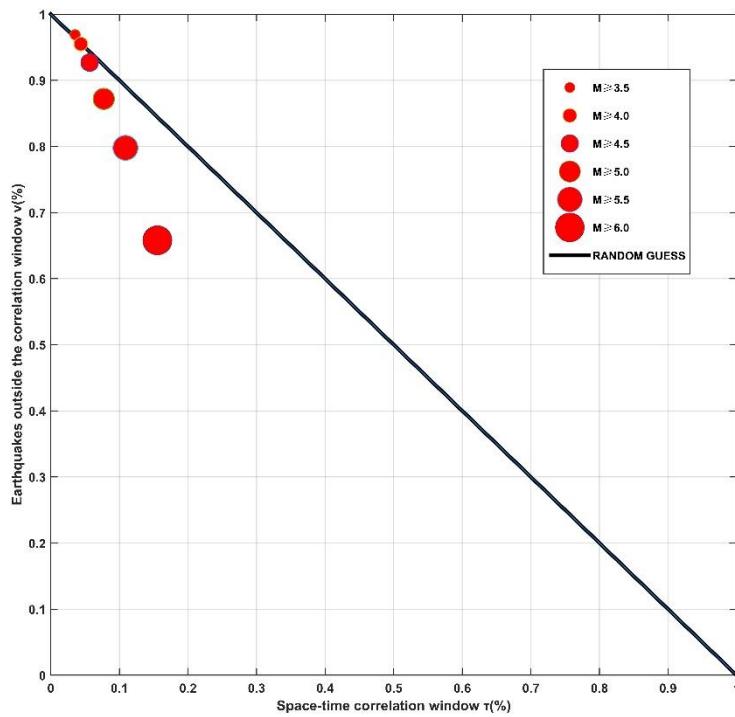
Fig. 10 Molchan error diagram analysis computed for different classes of magnitude and TIR anomalies during the study period (from 2002.09 to 2018.03); the red circles refer to earthquakes that occurred before and after the appearance of TIR anomalies.
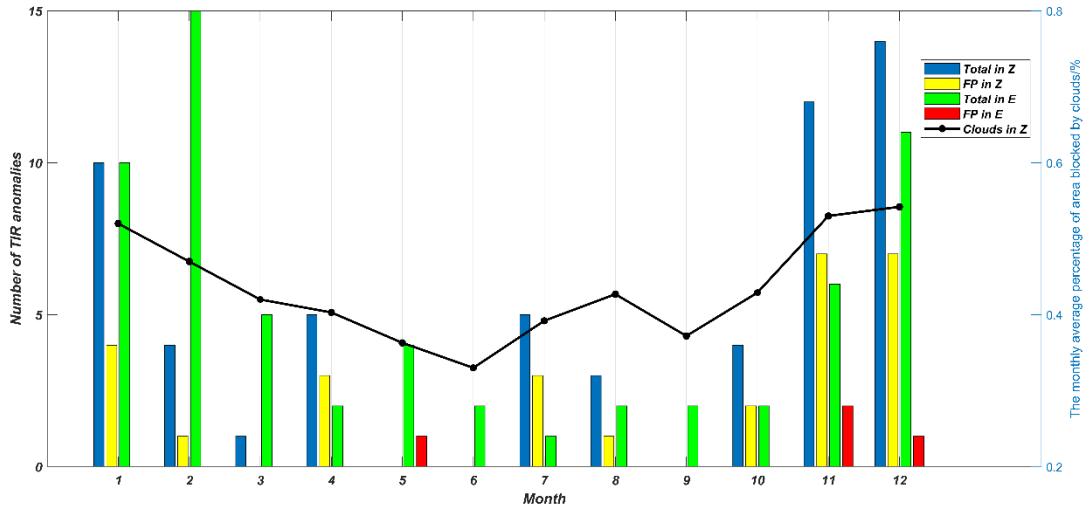
Fig. 11 The monthly average percentage of the area not blocked by clouds in Zhang's study region, i.e., that of this study. The bar chart presents the numbers of various types of TIR anomaly. 'Total in Z' is the total number of TIR anomalies in this study; 'FP in Z' is the number of TIR anomalies that do not correspond to any earthquakes in this study; 'Total in E' is the total number of TIR anomalies in Eleftheriou's study; 'FP in E' is the number of TIR anomalies that do not correspond to any earthquakes in Eleftheriou's study.

6. Conclusions

(1) Statistical analysis of 18 years' worth of data on the correlation between earthquakes and TIR anomalies indicate that 51.7% of TIR anomalies correspond to earthquakes of $M \geq 4.0$ in the Sichuan region, and the higher the M, the more likely it is that the earthquakes will correspond to TIR anomalies. The low PPV and TPR may be attributable to the large portions of the study region that are covered by clouds throughout the year.

(2) The low PPV and TPR suggest that the earthquake prediction potential of RST using MODIS LST data with regard to the Sichuan region is limited. For stronger earthquakes, with $M \geq 6.0$, although the false alarm rate is high, the missing rate is relatively low. RST was applied to the study area and was found to have significant predictive potential with regard to strong earthquakes.

(3) There is no obvious correlation between earthquakes of $M < 5.0$ and the TIR anomalies extracted using RST and MODIS LST data in the Sichuan region. However, the underlying causes of this situation merit further investigation.

(4) The RST proposed in this study and in Eleftheriou's study is still considerably affected by cloud cover and seasonal influences. It is necessary to improve and optimize algorithms and statistical methods that facilitate the exclusion of cloud and seasonal influences.

5   Reference

Aliano, C., Corrado, R., Filizzola, C. and Pergola, N. Robust Satellite Techniques (RST) for Seismically Active Areas Monitoring: the Case of 21st May, 2003 Boumerdes/Thenia (Algeria) Earthquake. Analysis of Multi-temporal Remote Sensing Images, 2007. MultiTemp 2007. International Workshop on the, 2007.

10   Aliano, C., Corrado, R., Filizzola, C., Genzano, N., Pergola, N., Tramutoli, V. "Robust TIR satellite tecniques for monitoring earthquake active regions: limits, main achievements and perspectives." Ann Geophys 51:303-317, 2008.

Bellaoui, M., Hassini, A. and Kada, B. "Pre-seismic Anomalies in Remotely Sensed Land Surface Temperature measurements: the Case Study of 2003 Boumerdes Earthquake." Advances in Space

15   Research **59**(10), 2017.

Blackett, M., Wooster, M. J. and Malamud, B. D. "Correction to “Exploring land surface temperature earthquake precursors: A focus on the Gujarat (India) earthquake of 2001." Geophysical Research Letters **38**(18): L15303, 2011.

Filizzola, C., Pergola, N., Pietrapertosa, C. and Tramutoli, V. "Robust satellite tecniques for seismically

20   active areas monitoring: a sensitvity analysis on September 7, 1999 Athens's earthquake." Phys Chem Earth 29: 517-527, 2004.

Eleftheriou, A., Filizzola, C., Genzano, N., Lacava, T., Lisi, M., Paciello, R., Pergola, N., Vallianatos, F. and Tramutoli, V. "Long-Term RST Analysis of Anomalous TIR Sequences in Relation with Earthquakes Occurred in Greece in the Period 2004–2013." Pure & Applied Geophysics **173**(1): 285-303, 2016.

25   Genzano, N., Aliano, C., Corrado, R., Filizzola, C., Lisi, M., Mazzeo, G., Paciello, R., Pergola, N., Tramutoli, V. "RST analysis of MSG-SEVIRI TIR radiances at time of the Abruzzo 6 April 2009 earthquake." Nat. Hazards Earth Syst Sci 9:2073-2084, 2009.

Genzano, N., Corrado, R., Coviello, I., Grimaldi, C. S. L., Filizzola, C., Lacava, T., Lisi, M., Marchese, F., Mazzeo, G. and Paciello, R. A multi-sensors analysis of RST-based thermal anomalies in the case of the

30   Abruzzo earthquake. Geoscience and Remote Sensing Symposium, 2010.

Genzano, N., Filizzola, C., Paciello, R., Pergola, N. and Tramutoli, V. "Robust Satellite Techniques (RST) for monitoring earthquake prone areas by satellite TIR observations: The case of 1999 Chi-Chi earthquake (Taiwan)." Journal of Asian Earth Sciences **114**(2): 289-298, 2015.

Gorny, V. I., Salman, A. G. and Tronin, A. A. "The earth outgoingIRradiation as an indicator of seismic

35   activity." 1988.

Lisi, M., Filizzola, C., Genzano, N. and Grimaldi, C. S. L. "A study on the Abruzzo 6 April 2009 earthquake by applying the RST approach to 15 years of AVHRR TIR observations." Natural Hazards & Earth System Sciences **10**(2): 395-406, 2010.

Ouzounov, D. and Freund, F. "Mid-infrared emission prior to strong earthquakes analyzed by remote

40   sensing data." Advances in Space Research **33**(3): 268-273, 2004.

Pergola, N., Aliano, C., Coviello, I. and Filizzola, C. "Using RST approach and EOS-MODIS radiances for monitoring seismically active regions: a study on the 6 April 2009 Abruzzo earthquake." Natural Hazards

& Earth System Sciences **10**(2): 239-249, 2010.

Piroddi, L., Ranieri, G., Freund, F. and Trogu, A. "Geology, tectonics and topography underlined by L'Aquila earthquake TIR precursors." Geophysical Journal International **197**(3): 1532-1536, 2014.

Qiang, Z. J., Xu, X. D. and Dian, C. G. "Case 27 thermal infrared anomaly precursor of impending
5 earthquakes." Chinese Science Bulletin **149**(4): 159-171, 1991.

Saraf, A. K., Rawat, V., Choudhury, S., Dasgupta, S. and Das, J. "Advances in understanding of the mechanism for generation of earthquake thermal precursors detected by satellites." International Journal of Applied Earth Observation & Geoinformation **11**(6): 373-379, 2009.

Tramutoli, V. "Robust AVHRR techniques (RAT) for environmental monitoring: theory and applications."
10 Proc Spie **3496**(3496): 101-113, 1998.

Tramutoli, V. Robust Satellite Techniques (RST) for Natural and Environmental Hazards Monitoring and Mitigation: Theory and Applications. Analysis of Multi-temporal Remote Sensing Images, 2007. MultiTemp 2007. International Workshop on the, 2007.

Tramutoli, V. Robust Satellite Techniques (RST) for natural and environmental hazards monitoring and
15 mitigation: ten year of successful applications. International Symposium on Physical Measurements and Signatures, 2005.

Tramutoli, V., Aliano, C., Corrado, R., Filizzola, C., Genzano, N., Lisi, M., Martinelli, G. and Pergola, N. "On the possible origin of thermal infrared radiation (TIR) anomalies in earthquake-prone areas observed using robust satellite techniques (RST)." Chemical Geology **339**(2): 157-168, 2013.

20 Tramutoli, V., Bello, G. D., Pergola, N. and Piscitelli, S. "Robust satellite techniques for remote sensing of seismically active areas." Annals of Geophysics **44**(2): 295-312, 2001.

Tramutoli, V., Corrado, R., Filizzola, C., Genzano, N., Lisi, M., Paciello, R. and Pergola, N. "One year of RST based satellite thermal monitoring over two Italian seismic areas." Bollettino Di Geofisica Teorica Ed Applicata **56**(2): 275-294, 2015.

25 Tramutoli, V., Corrado, R., Filizzola, C., Genzano, N., Lisi, M. and Pergola, N. "From visual comparison to Robust Satellite Techniques: 30 years of thermal infrared satellite data analyses for the study of earthquake preparation phases." Bollettino Di Geofisica Teorica Ed Applicata **56**(2): 167-202, 2015.

Tramutoli, V., Cuomo, V., Filizzola, C., Pergola, N. and Pietrapertosa, C. "Assessing the potential of thermal infrared satellite surveys for monitoring seismically active areas: The case of Kocaell (Izmit)
30 earthquake, August 17, 1999." Remote Sensing of Environment **96**(3): 409-426, 2005.

Tronin, A. A. "Satellite thermal survey—a new tool for the study of seismoactive regions." International Journal of Remote Sensing **17**(8): 1439-1455, 1996.

Tronin, A. A., Hayakawa, M. and Molchanov, O. A. "Thermal IR satellite data application for earthquake research in Japan and China." Journal of Geodynamics **33**(4–5): 519-534, 2002.

35 Wang, L. "ANOMALOUS VARIATIONS OF GROUND TEMPERATURE BEFORE THE TANGSHAN AND HAICHENG EARTHQUAKES." Journal of Seismological Research, 1984.

Yang, L. M., Zhang, Y. and Zhang, F. F. "STUDY ON MUTUAL FEATURES OF MIDDLE EARTHQUAKES ACTIVITIES BEFORE MIDDLE-STRONG EARTHQUAKES IN EAST-SOUTHERN GANSU PROVINCE AND ITS NEIGHBOR REGIONS." Platean Earthquake Research, 2002.

40